Eur. Phys. J. D (2022)76:228
https://doi.org/10.1140/epjd/s10053-022-00528-x

THE EUROPEAN PHYSICAL JOURNAL D

Regular Article – Quantum Optics

Room-temperature polarization of individual nuclear spins in diamond via anisotropic hyperfine coupling and coherent population trapping

P. Jamonneau[1], A. Dréau[2], G. Hétet[3], J. F. Roch[1], J. R. Maze[4], and V. Jacques[2,a]

[1] Université Paris-Saclay, CNRS, ENS Paris-Saclay, Centrale Supélec, LuMIn, 91190 Gif-sur-Yvette, France
[2] Laboratoire Charles Coulomb, Université de Montpellier and CNRS, 34095 Montpellier, France
[3] Laboratoire Pierre Aigrain, CNRS, Université Pierre et Marie Curie, Université Paris Diderot and Ecole Normale Supérieure, 75005 Paris, France
[4] Institute of Physics, Pontificia Universidad Catolica de Chile, Santiago, Chile

Received 27 July 2022 / Accepted 11 October 2022

Abstract. We employ the electronic spin of a single nitrogen-vacancy (NV) defect in diamond to detect and control the quantum state of remote nuclear spins coupled by hyperfine interaction. More precisely, our work focuses on individual ^{13}C nuclei featuring a moderate hyperfine coupling strength ($\sim$ 1 MHz) with the NV's electron spin. Two different methods providing an efficient room-temperature polarization of these peculiar ^{13}C nuclear spins are described. The first one is based on a polarization transfer from the NV electron spin to the ^{13}C nucleus, which is mediated by the anisotropic component of the hyperfine interaction. The second one relies on coherent population trapping (CPT) within a Λ-type energy-level configuration in the microwave domain, which enables to initialize the ^{13}C nuclear spin in any quantum state superposition on the Bloch sphere. This CPT protocol is performed in an unusual regime for which relaxation from the excited level of the Λ-scheme is externally triggered by optical pumping and separated in time from coherent microwave excitations. For these two polarization techniques, we investigate the impact of optical illumination on the nuclear spin polarization efficiency. This work adds new methods to the quantum toolbox used for coherent control of individual nuclear spins in diamond, which might find applications in quantum metrology.

1 Introduction

The experimental demonstration of entanglement between two photons is a landmark contribution of Alain Aspect that led to the emergence of the second quantum revolution and to the development of quantum technologies [1]. Today, these technologies exploit a broad diversity of quantum systems that can be isolated and manipulated at the individual level. Among them, nuclear spins in solids stand out for their extremely long coherence time, which results from a high level of isolation from the environment. This property has opened many perspectives in quantum information science [2–5], metrology [6–8] and, more recently, quantum simulations [9]. Despite such interesting prospects, individual nuclear spins have long remained difficult to detect owing to their very low gyromagnetic ratio. A solution to this problem consists in using an ancillary single-electron spin as a quantum sensor allowing to probe remote nuclei coupled by hyperfine interaction [10–12]. A prominent example is the single-shot detection and coherent control of individual nuclear spins in diamond obtained by mapping their quantum states onto the electron spin of a single nitrogen-vacancy (NV) color center [13–17]. This atomic-sized impurity has a spin triplet ground state, which can be efficiently polarized by optical pumping, coherently manipulated with microwave magnetic fields and read-out through optically detected magnetic resonance methods [18]. Due to its long coherence time [19], the NV's electronic spin provides a robust interface to detect and control the quantum state of nuclear spins localized at neighboring lattice sites in the diamond matrix. During the last decade, these nuclei have been extensively used as memory qubits, both for advanced quantum information protocols [20–23] and for quantum sensing applications [24–27].

The NV's electronic spin is always coupled with the nucleus of the nitrogen atom constituting the defect, whose majority isotope ^{14}N ($>$ 99.6%) has a nuclear

Guest editors: David Clément, Philippe Grangier and Joseph Thywissen.

[a] e-mail: vincent.jacques@umontpellier.fr (corresponding author)

Published online: 28 November 2022

spin $I_N = 1$. Moreover, the lattice sites of the diamond crystal are randomly occupied by ^{13}C atoms ($I = 1/2$) with a natural isotopic content around 1.1%. These paramagnetic impurities constitute a dilute nuclear spin bath, whose fluctuations are responsible for the decoherence of the NV defect electron spin [28–31]. However, when a ^{13}C atom is sufficiently close to the NV center, the hyperfine interaction is strong enough to be resolved in electron spin resonance (ESR) spectra, thus allowing nuclear-spin selective control of the coupled quantum system [12–14]. Systematic studies of the hyperfine structure of individual NV defects have shown that the hyperfine coupling strength with nearby ^{13}C nuclei can only take discrete values, which correspond to different neighboring lattice sites in the diamond matrix [32–35]. To detect such ^{13}C atoms in ESR spectra, it is however necessary that the strength of the hyperfine coupling exceeds the spectral width of the magnetic resonance, which is intrinsically limited by the decoherence rate $\gamma_2^\star$ of the NV electron spin. For a high-purity diamond crystal with a natural content of ^{13}C isotope, $\gamma_2^\star \sim 200$ kHz [29]. As a result, only one or two strongly coupled ^{13}C are at best detected in the vicinity of a given NV defect [34], limiting the size of the quantum register to few qubits. A powerful approach to further increase the size of the quantum register is offered by dynamical decoupling spectroscopy [36–38], which enables to detect and control weakly coupled ^{13}C from the bath. Using such methods, up to ten spin qubits have been recently included in a diamond-based quantum register [39].

Any use of individual ^{13}C nuclear spin for quantum technologies requires first a reliable initialization of its quantum state. Depending on the strength of the hyperfine interaction, different nuclear spin polarization methods can be employed. For ^{13}C nuclei featuring a strong hyperfine coupling with the NV's electron spin (≥ 2 MHz), an efficient polarization can be obtained by exploiting an excited-state level anti-crossing of the NV defect [34,40]. In this case, electron-nuclear-spin flip-flops mediated by the hyperfine interaction in the NV's excited state lead to a transfer of electron spin polarization to the nuclear spin by optical pumping. Such a polarization transfer can also be obtained by using nuclear spin selective microwave excitations combined with an applied magnetic field providing a ^{13}C Larmor precession conditional on the NV electron spin state [14]. For weakly coupled ^{13}C (< 200 kHz), polarization is rather obtained through single-shot readout methods [17,21,41] or dynamical decoupling protocols [36].

In this work, we focus on individual ^{13}C with intermediate hyperfine coupling strengths (~ 1 MHz), for which the polarization techniques mentioned above are ineffective. We describe two different methods providing an efficient polarization of these peculiar ^{13}C nuclear spins under ambient conditions. The first one is based on a polarization transfer from the NV electron spin to the ^{13}C nucleus which is mediated by the anisotropic component of the hyperfine interaction [42–45]. The second one relies on coherent population trapping within a Λ-type energy-level configuration in the microwave domain [46], which enables to initialize the nuclear spin in any quantum state superposition on the Bloch sphere. For these two techniques, we investigate the impact of optical illumination on the nuclear spin polarization efficiency. This work adds new methods to the quantum toolbox used for coherent control of individual nuclear spins in diamond, which might find applications in quantum metrology [47].

The paper is organized as follows. In Sect. 2, we first introduce the Hamiltonian describing the electron spin of a single NV defect in diamond coupled by hyperfine interaction with a nearby ^{13}C nuclear spin and we give details about the experimental setup. We then describe in Sect. 3 the nuclear spin polarization protocol relying on the ^{13}C Larmor precession mediated by anisotropic hyperfine coupling. Section 4 is finally devoted to room-temperature initialization of a single nuclear spin via coherent population trapping methods.

2 Spin system

2.1 Spin Hamiltonian

We start by introducing the spin Hamiltonian describing a single NV defect coupled by hyperfine interaction with a nearby ^{13}C nuclear spin (Fig. 1a) [33,34].

The ground level of the NV defect is an electronic spin triplet ($S = 1$) with a characteristic zero-field splitting $D \sim 2.87$ GHz between a singlet state $m_s = 0$ ($|0_e\rangle$) and a doublet $m_s = \pm 1$ ($|\pm 1_e\rangle$) [18]. Here m_s denotes the spin projection along the intrinsic quantization axis (z) of the NV defect, which corresponds to the [111] crystal axis joining the nitrogen and the vacancy. For a magnetic field B applied along this axis, the ground-state spin Hamiltonian in frequency units reads

$$\hat{\mathcal{H}}_0 = D\hat{S}_z^2 - \gamma_e B\hat{S}_z \tag{1}$$

where $\gamma_e \approx -2.8$ MHz/G is the electronic spin gyromagnetic ratio. When a neighboring lattice site of the NV defect is occupied by a ^{13}C nuclear spin ($I = 1/2$), the spin Hamiltonian describing the coupled spin system is given by

$$\hat{\mathcal{H}} = \hat{\mathcal{H}}_0 - \gamma_n B\hat{I}_z + \hat{\mathbf{S}} \cdot \mathcal{A} \cdot \hat{\mathbf{I}} \tag{2}$$

where $\gamma_n = 1.07$ kHz/G is the gyromagnetic ratio of the ^{13}C nuclear spin and $\mathcal{A}$ denotes the hyperfine interaction tensor. In the secular approximation for the electron spin, this Hamiltonian simplifies as

$$\hat{\mathcal{H}} = \hat{\mathcal{H}}_0 - \gamma_n B\hat{I}_z + \hat{S}_z\mathcal{A}_{zz}\hat{I}_z \tag{3}$$

$$+\frac{1}{2}\mathcal{A}_{ani}\hat{S}_z(e^{-i\phi}\hat{I}_+ + e^{i\phi}\hat{I}_-) \tag{4}$$

where $\hat{I}_\pm = \hat{I}_x \pm i\hat{I}_y$ are the nuclear spin ladder operators, $\mathcal{A}_{ani} = (\mathcal{A}_{zx}^2 + \mathcal{A}_{zy}^2)^{1/2}$ is the anisotropic compo-

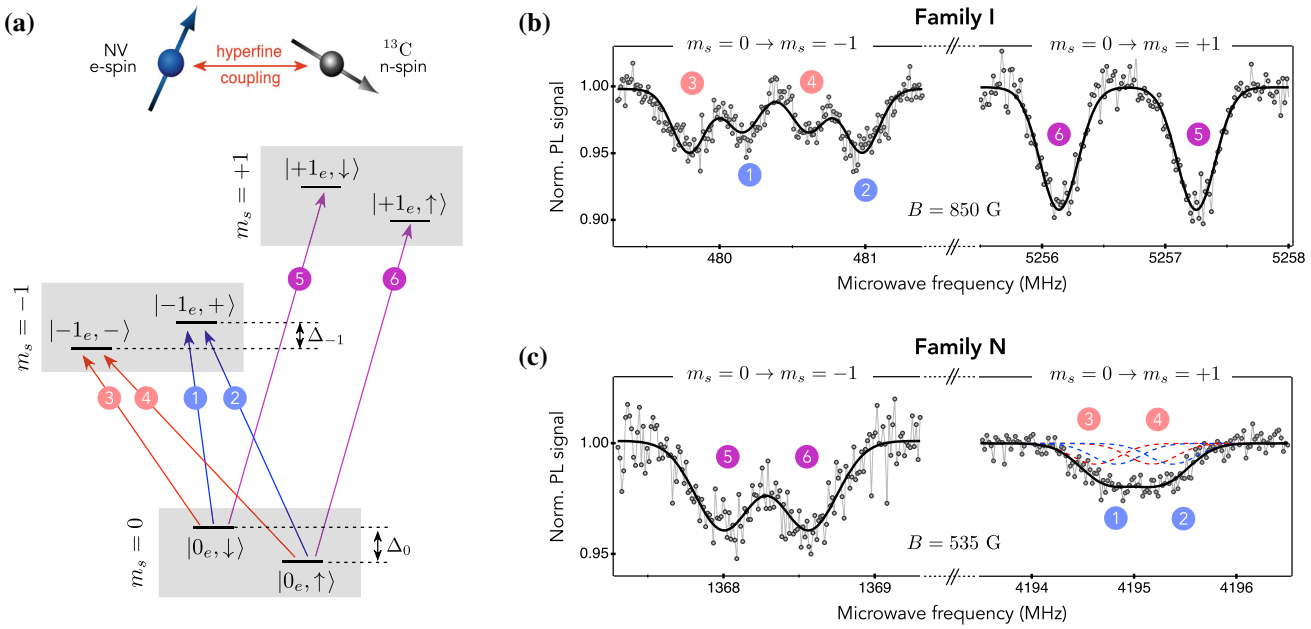

Fig. 1 **a** Energy-level structure of a single NV defect in diamond coupled by hyperfine interaction with a nearby ^{13}C nuclear spin. All notations are defined in the main text. In this diagram, we consider $\mathcal{A}_{zz} < 0$ and $\gamma_n B + \mathcal{A}_{zz} \sim 0$, leading to nuclear spin mixing in the $m_s = -1$ electron spin manifold. The ESR transitions are labeled from ① to ⑥. **b** ESR spectrum recorded at $B = 850$ G for a single NV defect coupled with a ^{13}C nuclear spin from 'family I.' **c** Same experiment performed at $B = 535$ G for a single NV defect coupled with a ^{13}C nuclear spin from 'family N.' Here $\mathcal{A}_{zz} > 0$ such that nuclear spin mixing occurs in the $m_s = +1$ electron spin manifold

nent of the hyperfine interaction, and $\tan\phi = \mathcal{A}_{zy}/\mathcal{A}_{zx}$. We note that the hyperfine interaction with the intrinsic ^{14}N nuclear spin ($I_N = 1$) of the NV defect is not included in the Hamiltonian since it is not playing any role in the experiments reported in this work. We thus consider a fixed ^{14}N nuclear spin projection, e.g., $m_{I_N} = +1$.

In the following we assume that $\mathcal{A}_{zz} < 0$, and the eigenstates of the $\hat{I}_z$ operator are denoted as $|\uparrow\rangle$ and $|\downarrow\rangle$. In the $m_s = 0$ electron spin subspace, the eigenstates of the coupled spin system are $|0_e,\uparrow\rangle$ and $|0_e,\downarrow\rangle$ with eigenenergies separated by $\Delta_0 = \gamma_n B$ (Fig. 1a). In the $m_s = -1$ manifold, the eigenstates are expressed as

$$|-1_e,+\rangle = \cos(\theta/2)|-1_e,\downarrow\rangle - \sin(\theta/2)e^{-i\phi}|-1_e,\uparrow\rangle$$
$$|-1_e,-\rangle = \sin(\theta/2)e^{i\phi}|-1_e,\downarrow\rangle + \cos(\theta/2)|-1_e,\uparrow\rangle$$

with

$$\tan\theta = \frac{\mathcal{A}_{ani}}{\gamma_n B + \mathcal{A}_{zz}}. \tag{5}$$

and eigenenergies separated by

$$\Delta_{-1} = \sqrt{\mathcal{A}_{ani}^2 + (\gamma_n B + \mathcal{A}_{zz})^2}. \tag{6}$$

The nuclear spin mixing parameter θ can be experimentally controlled by tuning the magnetic field B applied along the NV defect axis. When $\gamma_n B + \mathcal{A}_{zz} \sim 0$, i.e., when $\theta \sim \pi/2$ and $\Delta_{-1} \sim \mathcal{A}_{ani}$, four ESR transitions can be driven from $m_s = 0$ to $m_s = -1$. These transitions are labeled from ① to ④ in Fig. 1a. Such a coupled spin configuration corresponds to a double Λ-scheme in the microwave domain that will be used to perform coherent population trapping of a single nuclear spin in Sect. 4.

In the $m_s = +1$ electron spin manifold, the eigenstates of the coupled spin system are given by

$$|+1_e,+'\rangle = \cos(\theta'/2)|+1_e,\downarrow\rangle + \sin(\theta'/2)e^{-i\phi}|+1_e,\uparrow\rangle$$
$$|+1_e,-'\rangle = -\sin(\theta'/2)e^{i\phi}|+1_e,\downarrow\rangle + \cos(\theta'/2)|+1_e,\uparrow\rangle$$

where

$$\tan\theta' = \frac{\mathcal{A}_{ani}}{\gamma_n B - \mathcal{A}_{zz}}. \tag{7}$$

Assuming $\mathcal{A}_{zz} < 0$, the condition $|\mathcal{A}_{zz} - \gamma_n B| \gg \mathcal{A}_{ani}$ is always fulfilled, so that $\theta' \approx 0$ and

$$|+1_e,+'\rangle = |+1_e,\downarrow\rangle \tag{8}$$
$$|+1_e,-'\rangle = |+1_e,\uparrow\rangle. \tag{9}$$

The ^{13}C nuclear spin projections are therefore identical in the $m_s = 0$ and $m_s = +1$ electron spin manifolds, and only two nuclear-spin conserving ESR transitions can be driven by a microwave excitation. These transitions are labeled ⑤ and ⑥ in Fig. 1a. In the following, such ESR transitions without nuclear spin mixing will

be used to evaluate the efficiency of nuclear spin polarization.

We note that for a ^{13}C nuclear spin with $\mathcal{A}_{zz} > 0$, nuclear spin mixing is instead obtained in the $m_s = +1$ electron spin manifold.

2.2 Experimental details

We investigate native NV defects hosted in a high-purity diamond crystal grown by chemical vapor deposition (Element 6) with a natural abundance of ^{13}C isotopes (1.1%). Individual NV defects are optically isolated at room temperature with a scanning confocal microscope using a laser excitation at 532 nm whose power is set at the saturation intensity of the NV's optical transition. Under optical illumination, the NV defect is efficiently polarized in the $m_s = 0$ ground state. In addition, it exhibits a spin-dependent PL signal enabling electron spin readout through optically detected magnetic resonance methods [18,48]. In this work, these properties will be exploited to polarize and readout individual ^{13}C nuclear spins. A permanent magnet mounted on a three-axis translation stage is used to apply a static magnetic field along the NV defect axis and ESR transitions are driven by a microwave excitation applied through a copper microwire deposited on the crystal surface. Optically detected ESR spectra are recorded by monitoring the spin-dependent PL signal of the NV defect while sweeping the microwave frequency. More details about the experimental setup can be found in Ref. [49].

All experiments reported in this work are performed on two different NV defects. The first one is coupled to a ^{13}C nuclear spin localized on a neighboring lattice site referred to as 'family I' in Ref. [34], whose hyperfine interaction is characterized by a longitudinal component $\mathcal{A}^{\mathrm{I}}_{zz} \sim -1$ MHz. Figure 1b shows the ESR spectrum recorded for this NV defect at a magnetic field $B = 850$ G, i.e., such that $\gamma_n B + \mathcal{A}^{\mathrm{I}}_{zz} \sim 0$. As expected, the $m_s = 0 \rightarrow m_s = -1$ transition features four hyperfine lines owing to nuclear spin mixing induced by the anisotropic component of the hyperfine interaction. The second NV defect studied below is coupled to a ^{13}C nuclear spin belonging to 'family N' that correspond to $\mathcal{A}^{\mathrm{N}}_{zz} \sim +0.5$ MHz [34]. In this case, nuclear spin mixing occurs in the $m_s = +1$ manifold. The ESR spectrum recorded at $B = 535$ G is shown in Fig. 1c. Although the four hyperfine lines cannot be properly resolved, the observed broadening of the $m_s = 0 \rightarrow m_s = +1$ transition is a signature of nuclear spin mixing.

3 Nuclear-spin polarization via anisotropic hyperfine coupling

3.1 Nuclear spin Larmor precession

The anisotropic component of the hyperfine interaction can be exploited to perform coherent manipulation of the nuclear spin [42–44]. To illustrate this, we apply the experimental sequence sketched in Fig. 2a to the NV defect coupled with a ^{13}C belonging to 'family I' ($\mathcal{A}_{zz} < 0$). A laser pulse is first used to initialize the electron spin in $m_s = 0$ by optical pumping. A nuclear-spin selective microwave π-pulse is then applied to transfer the population with nuclear spin state $|\uparrow\rangle$ from the $m_s = 0$ to the $m_s = -1$ electron spin manifold. After this microwave pulse, the nuclear spin projection is tilted with respect to its quantization axis in the $m_s = -1$ subspace. As a result, it starts to precess under the effect of the anisotropic hyperfine interaction with a characteristic Larmor frequency

$$\nu_{\mathrm{R}} = \Delta_{-1} = \sqrt{\mathcal{A}^2_{ani} + (\mathcal{A}_{zz} + \gamma_n B)^2}. \qquad (10)$$

Following a free precession time τ, a second microwave π-pulse is applied to bring the remaining population in $|\uparrow\rangle$ from $m_s = -1$ to $m_s = 0$. A laser pulse is finally

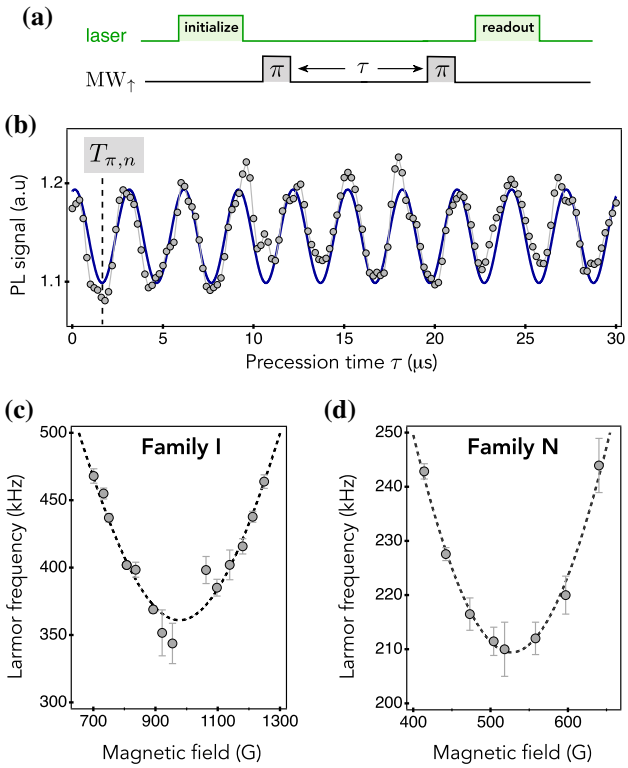

Fig. 2 **a** Pulse sequence used to detect the nuclear spin Larmor oscillation induced by the anisotropic component of the hyperfine interaction. The microwave π-pulse, which duration is set to $T_{\pi,e} = 2$ μs, selectively excites the nuclear spin projection $|\uparrow\rangle$ (i.e., transitions ② and ④ shown in Fig. 1a). **b** PL signal recorded during the readout laser pulse as a function of the free precession time τ. The blue solid line is data fitting with a cosine function. The free precession time corresponding to an optimal nuclear spin flip is referred to as $T_{\pi,n}$. **c**,**d** Larmor frequency as a function of the magnetic field for a ^{13}C nuclear spin from 'family I'(**c**) and from 'family N' (**d**). The black dashed lines are data fitting with Eq. (10)

used to readout the population in $m_s = 0$ through a measurement of the spin-dependent PL signal. This sequence is repeated continuously to average the PL signal while increasing the free precession time.

The result of this experiment performed at $B \sim 900$ G is depicted in Fig. 2b. We observe an oscillation of the PL signal that corresponds to a Larmor precession at the frequency ν_R between the $|\uparrow\rangle$ and $|\downarrow\rangle$ nuclear spin states in the $m_s = -1$ spin subspace. The evolution of the Larmor frequency with the magnetic field is shown in Fig. 2c. By fitting the data with Eq. (10), we infer the hyperfine interaction components for a ^{13}C nuclear spin belonging to 'family I,' $\mathcal{A}^{\mathrm{I}}_{zz} = -1047 \pm 6$ kHz and $\mathcal{A}^{\mathrm{I}}_{ani} = 360 \pm 3$ kHz. These values are in fair agreement with previous experimental work using different measurement methods [34] and with *ab initio* theoretical calculations [35]. The same experiments were also performed for a single NV defect coupled to a ^{13}C from 'family N' (Fig. 2d), leading to $\mathcal{A}^{\mathrm{N}}_{zz} = +565 \pm 7$ kHz and $\mathcal{A}^{\mathrm{N}}_{ani} = 209 \pm 5$ kHz.

Besides providing an alternative method to characterize the components of the hyperfine interaction, these measurements enable to infer the free precession time $T_{\pi,n}$ that corresponds to a nuclear spin inversion induced by the anisotropic hyperfine coupling (Fig. 2b). Obtaining an optimal nuclear spin flip involves several experimental constraints. First the magnetic field must fulfill the condition $\gamma_n B + \mathcal{A}_{zz} \sim 0$ to achieve maximum nuclear spin mixing, thus optimizing the amplitude of the Rabi oscillation. Second, the microwave π-pulse has to selectively excite a given nuclear spin projection. To drive the nuclear spin state $|\uparrow\rangle$ (resp. $|\downarrow\rangle$), the π-pulse must excite simultaneously the ESR transitions ② and ④ (resp. ① and ③). Such a nuclear spin selectivity is fulfilled if the π-pulse duration $T_{\pi,e}$ is such that $\Delta_{-1} \ll T^{-1}_{\pi,e} \ll \Delta_0$ (see Fig. 1a). For a magnetic field maximizing nuclear spin mixing, this condition can be expressed as

$$\mathcal{A}_{ani} \ll T^{-1}_{\pi,e} \ll |\mathcal{A}_{zz}| \tag{11}$$

which is hard to satisfy for ^{13}C nuclear spins featuring a weak hyperfine coupling strength. For the experiments described above, the microwave power was adjusted to obtain a π-pulse duration $T_{\pi,e} = 2$ μs that corresponds to a spectral width around 500 kHz. Given the hyperfine coupling strength considered in this work, Eq. (11) is not perfectly satisfied in our experiments, leading to a reduced fidelity of the nuclear spin flip. This is one of the limiting factor of the nuclear spin polarization protocol described in the next section.

3.2 Nuclear spin polarization

The experimental sequence used to achieve nuclear spin polarization is depicted in Fig. 3a. Starting with the electron spin initialized in $m_s = 0$, a nuclear spin-selective microwave π-pulse is followed by a free precession time $T_{\pi,n}$ which results in a nuclear spin flip in the $m_s = -1$ electron spin subspace. Such a nuclear spin flip is then transferred to the $m_s = 0$ manifold through optical pumping with a green laser pulse. If the selective microwave π-pulse is applied on the nuclear spin projection $|\downarrow\rangle$ (resp. $|\uparrow\rangle$), this simple sequence leads to nuclear spin pumping in state $|\uparrow\rangle$ (resp. $|\downarrow\rangle$). In order to measure the resulting polarization without disturbing it, we perform pulsed ESR spectroscopy of the hyperfine transitions without nuclear spin mixing, which are labeled ⑤ and ⑥ in Fig. 1. To this end, the nuclear spin polarization step is followed by a microwave π-pulse and a readout laser pulse (Fig. 3a). ESR spectra are recorded by continuously repeating the whole sequence while sweeping the frequency of the readout microwave π-pulse across the transitions ⑤ and ⑥, and monitoring the spin-dependent PL signal.

The resulting ESR spectra are gathered in Fig. 3b for the NV defect coupled to a ^{13}C nuclear spin from 'family I.' When the nuclear spin polarization step is not introduced in the experimental sequence, the amplitudes of the ESR transitions ⑤ and ⑥ are identical (top panel), showing that the nuclear spin is in a thermal state with equal populations in $|\uparrow\rangle$ and $|\downarrow\rangle$, as expected. By including the polarization step, one of the ESR lines almost cancels out whereas the amplitude of the other becomes two times higher, revealing an efficient nuclear spin polarization. As discussed above, the nuclear spin can be polarized either in state $|\uparrow\rangle$ (middle panel) or in state $|\downarrow\rangle$ (bottom panel), by changing the nuclear-spin selectivity of the microwave excitation. As shown in Fig. 3c, similar results are obtained for the ^{13}C nuclear spin from 'family N,' thus illustrating the generality of the method.

The probability $\mathcal{P}_{|\uparrow(\downarrow)\rangle}$ to find the nuclear spin in state $|\uparrow(\downarrow)\rangle$ can be measured as

$$\mathcal{P}_{|\uparrow(\downarrow)\rangle} = \frac{\mathcal{I}_{|\uparrow(\downarrow)\rangle}}{\mathcal{I}_{|\downarrow\rangle} + \mathcal{I}_{|\uparrow\rangle}} \tag{12}$$

where $\mathcal{I}_{|\uparrow(\downarrow)\rangle}$ is the integral of the ESR line corresponding to the nuclear spin state $|\uparrow(\downarrow)\rangle$. For the ^{13}C nuclear spin from 'family I,' we obtain $\mathcal{P}^{\mathrm{I}}_{|\uparrow\rangle} = 84 \pm 3\%$ and $\mathcal{P}^{\mathrm{I}}_{|\downarrow\rangle} = 83 \pm 3\%$. The polarization is slightly less efficient for 'family N,' $\mathcal{P}^{\mathrm{N}}_{|\uparrow\rangle} = 78 \pm 3\%$ and $\mathcal{P}^{\mathrm{N}}_{|\downarrow\rangle} = 76 \pm 3\%$, because Eq. (11) is more difficult to fulfill for weakly coupled ^{13}C nuclei.

The nuclear spin polarization efficiency is governed by several parameters of the spin system. First, it is limited by the electron spin polarization efficiency of the NV defect under optical pumping [50], a parameter measured around 90% at room temperature [51]. Besides this intrinsic limit, the steady-state nuclear spin polarization obtained in our experiments is linked to (i) the selectivity of the microwave excitation, (ii) the efficiency of the nuclear spin flip induced by the anisotropic hyperfine interaction and (iii) the fidelity of its transfer to the $m_s = 0$ electron spin manifold by optical pumping. The laser pulse used for this transfer is known to depolarize the nuclear spin during optical cycles [14,44,52], leading to an overall reduction of

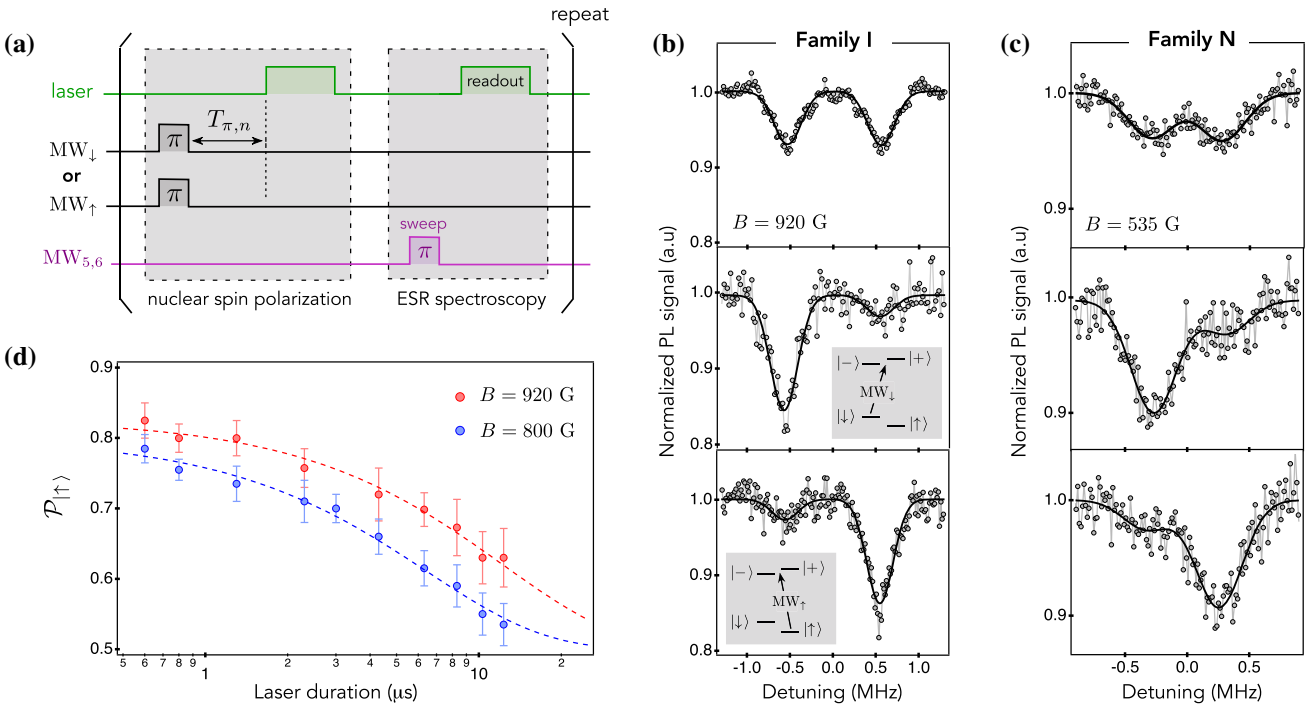

Fig. 3 **a** Nuclear spin polarization and readout sequence. **b**,**c** Polarization of a ^{13}C nuclear spin from 'family I' (**b**) and from 'family N' (**c**). The top panels correspond to the ESR spectra obtained without applying the nuclear spin polarization step. The middle (resp. bottom) panels show the ESR spectra obtained by including the polarization step with a microwave π-pulse exciting selectively the nuclear spin projection $|\downarrow\rangle$ (resp. $|\uparrow\rangle$). Solid lines are data fitting with Gaussian functions. The duration of the laser pulses used for polarization transfer and spin readout are set to 300 ns. **d** Probability $\mathcal{P}_{|\uparrow\rangle}$ plotted as a function of the total duration T_{tot} of the laser pulses used in the experimental sequence. The measurements are performed for the ^{13}C from 'family I' at two different magnetic fields. The data are plotted on a semi-log scale

the polarization efficiency. Such an optically induced nuclear spin relaxation also occurs during the laser pulse employed for polarization readout. To illustrate this effect, the probability $\mathcal{P}_{|\uparrow\rangle}$ was measured while increasing the total duration T_{tot} of the laser pulses used in the experimental sequence. The results obtained at two different magnetic fields for the ^{13}C from 'family I' are shown in Fig. 3d. We observe an exponential decrease of the nuclear spin polarization with T_{tot}. We note that the duration of each laser pulse cannot be reduced below ~ 300 ns in order to ensure both efficient polarization transfer and spin readout [49]. In addition, we observe that the polarization efficiency vanishes faster when the magnetic field is detuned from the condition $\gamma_n B + \mathcal{A}_{zz} \sim 0$, owing to a reduced fidelity of the nuclear spin flip in the $m_s = -1$ manifold. A more quantitative analysis of nuclear spin relaxation under optical illumination will be given in Sect. 4.3.

The polarization protocol described above makes it possible to initialize the nuclear spin state either in state $|\uparrow\rangle$ or in state $|\downarrow\rangle$. To obtain full control over the nuclear spin state, it is however necessary to prepare any coherent superposition on the Bloch sphere. Although this can be achieved through coherent manipulation of the nuclear spin state with a resonant radio-frequency excitation, we will describe in the next section an alternative approach based on coherent population trapping methods.

4 Nuclear spin polarization via coherent population trapping with controlled dissipation

4.1 Coherent population trapping of a single nuclear spin

Coherent population trapping (CPT) is a quantum interference effect that occurs in three-level quantum systems featuring a Λ-type configuration, i.e., with two fundamental levels coupled to the same excited level. The simultaneous coherent excitation of the two transitions leads to the pumping into a coherent superposition of the fundamental levels, which is commonly referred to as *dark state* because it is perfectly decoupled from the excitation of the quantum system [53]. Since its discovery in the seventies [54–56], CPT has found numerous applications in atomic physics, from laser cooling of atoms and molecules [57,58], to metrology [59,60] and quantum information storage [61,62]. More recently, this powerful method has been extended to various solid-state quantum systems including opti-

cally active electron spin impurities [63–65] and superconducting circuits [66,67].

Below, we make use of CPT methods to polarize a single ^{13}C nuclear spin in diamond at room temperature [46]. All the experiments described in this section make use of a single NV defect coupled with a ^{13}C nuclear spin from 'family I' at a magnetic field $B = 850$ G. As discussed in Sect. 2.1, nuclear spin mixing induced by the anisotropic hyperfine interaction results in two Λ-level configurations in the microwave domain (Fig. 1a). One of these Λ-level structures $\{|0_e,\uparrow\rangle, |0_e,\downarrow\rangle, |-1_e,+\rangle\}$ can be isolated and its ESR transitions coherently driven with two microwave excitations, MW_1 and MW_2. As sketched in Fig. 4a, the frequency of MW_1 is set on resonance while MW_2 is detuned by δ. When the two-photon resonance condition $\delta = 0$ is satisfied, the eigenstates of the coupled spin system are given by [53]

$$|B\rangle = \frac{1}{\sqrt{\Omega_1^2+\Omega_2^2}}\left(\Omega_1|0_e,\downarrow\rangle + \Omega_2|0_e,\uparrow\rangle\right) \quad (13)$$

$$|D\rangle = \frac{1}{\sqrt{\Omega_1^2+\Omega_2^2}}\left(\Omega_2|0_e,\downarrow\rangle - \Omega_1|0_e,\uparrow\rangle\right) \quad (14)$$

where Ω_1 and Ω_2 are the Rabi frequencies characterizing the strength of the microwave coupling on each branch of the Λ-scheme. The dark state $|D\rangle$ is perfectly decoupled from the microwave excitations. Conversely, the population of the bright state $|B\rangle$ is efficiently coupled to the $|-1_e,+\rangle$ level with an effective Rabi frequency $\Omega = \sqrt{\Omega_1^2+\Omega_2^2}$, and then partially transferred to the dark state by relaxation (Fig. 4b). After several excitation cycles, the system is thus trapped in the dark state. The relaxation process in atomic systems is commonly provided by spontaneous emission. For our coupled spin system, relaxation is rather controlled externally by applying a laser pulse which triggers the decay of populations from the $|-1_e,+\rangle$ states towards $|D\rangle$ and $|B\rangle$ in the $m_s = 0$ manifold (Fig. 4b) [46].

CPT of a single nuclear spin is revealed by recording an ESR spectrum while applying the experimental sequence sketched in Fig. 4c. The two branches of the Λ-scheme are simultaneously excited with two microwave pulses to obtain a quantum interference between the transition probabilities. A laser pulse is subsequently applied both to trigger relaxation of the spin system into the dark state and to perform electron spin readout by recording the spin dependent PL signal. The laser pulse duration is set to $T_L = 300$ ns in order to optimize the readout contrast while minimizing nuclear spin dephasing induced by optical cycles. By repeating continuously this simple sequence, an ESR spectrum can be recorded by monitoring the PL signal while sweeping the detuning δ across the resonance (Fig. 4c). The observation of a highly contrasted dip at two-photon resonance $\delta = 0$ indicates an efficient polarization of the spin system in the dark state. Interestingly, it was shown in a previous work that the composition of the dark state can be modified by changing Ω_1 and Ω_2 [see Eq. (14)], providing an efficient way to directly prepare the nuclear spin in any quantum state superposition on the Bloch sphere [46]. In the following sections, we investigate the dynamics of nuclear spin dephasing induced by the laser pulse that is employed to trigger relaxation in the Λ-level configuration.

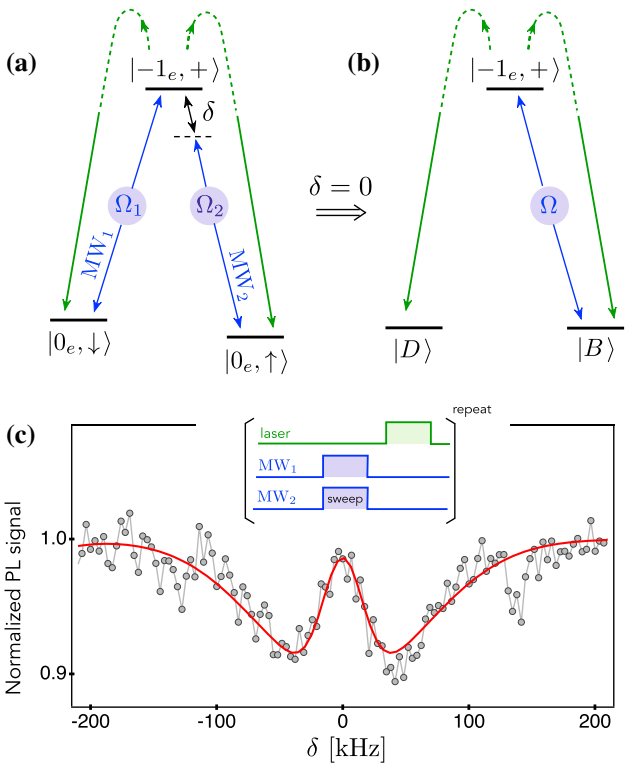

Fig. 4 **a** Λ-level configuration in the microwave domain. **b** Sketch illustrating the coupling between the eigenstates of the Λ scheme at the two-photon resonance condition $\delta = 0$. All notations are defined in the main text. The relaxation from the excited level $|-1_e,+\rangle$ is triggered by a green laser excitation (green arrows). **c** ESR spectrum recorded by applying the pulse sequence shown in inset with a duration of the laser pulse $T_L = 300$ ns. The dip observed at $\delta = 0$ is the signature of CPT in the dark state

4.2 Rabi oscillations within the Λ-scheme

To optimize the efficiency of dark state pumping, we first perform Rabi oscillations within the Λ-level configuration using the sequence sketched in Fig. 5a. Starting with the electron spin polarized in the $m_s = 0$ subspace and the ^{13}C nuclear spin in a thermal state, we apply simultaneously the two microwaves excitations at two-photon resonance $\delta = 0$ during a time τ. A laser pulse is then used for optical readout of the electron spin state. The duration of this laser pulse is set to 100 μs in order to start the next sequence with the nuclear spin reset to a thermal distribution. This measurement is repeated for different durations of the microwave pulse to reveal the Rabi oscillation at frequency $\Omega = \sqrt{\Omega_1^2+\Omega_2^2}$ between the levels $|B\rangle$ and

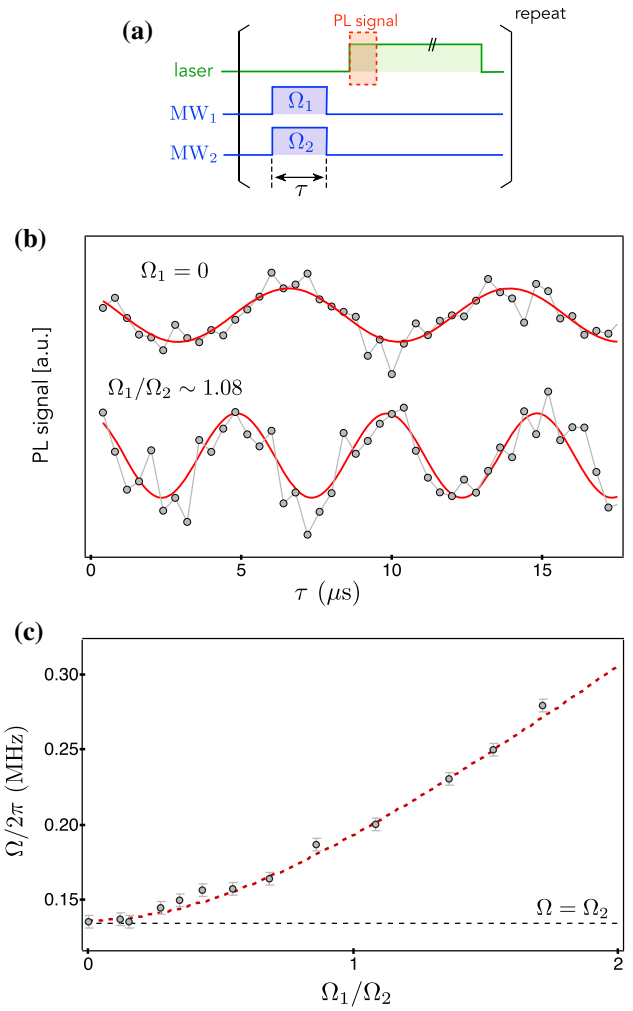

Fig. 5 **a** Pulse sequence used to record Rabi oscillations within the Λ-scheme. The PL signal is integrated during the first 300 ns of the laser pulse, whose duration is fixed to 100 μs in order to reset the nuclear spin in a thermal state at the end of the sequence. **b** PL signal plotted as a function of the duration τ of the dual microwave excitation. The top panel is obtained for $\Omega_1 = 0$ and the bottom panel for $\Omega_1/\Omega_2 = 1.08$. Solid lines are data fitting with cosine functions. The data are vertically shifted for the sake of clarity. **c** Evolution of the effective Rabi frequency $\Omega/2\pi$ as a function of Ω_1/Ω_2. The red dashed line corresponds to $\Omega = \Omega_2\sqrt{1+(\Omega_1/\Omega_2)^2}$

$|-1_e,+\rangle$. The experiment is reproduced by tuning the Rabi frequency Ω_1 while keeping Ω_2 constant.

Figure 5b shows the results obtained for two different values of Ω_1. The top curve is recorded for $\Omega_1 = 0$, such that $|B\rangle = |0_e,\uparrow\rangle$ and $|D\rangle = |0_e,\downarrow\rangle$. From these data, we infer $\Omega/2\pi = \Omega_2/2\pi = 136 \pm 4$ kHz. The bottom curve is recorded for $\Omega_1 \sim \Omega_2$, leading to $\Omega/2\pi = 200 \pm 5$ kHz. It corresponds to an increase of the Rabi frequency by a factor $\sqrt{2}$, which is a characteristic signature of the quantum interference between the transition probabilities in the Λ-level configuration. The effective Rabi frequency Ω is plotted as a function of Ω_1/Ω_2 in Fig. 5c. The experimental results are very well reproduced by the theoretical prediction $\Omega = \sqrt{\Omega_1^2+\Omega_2^2}$.

Such measurements of the Rabi oscillation enable us to infer the duration of a dual microwave π-pulse which maximizes population transfer to the excited level of the Λ-scheme. Below, all measurements are performed with such a π-pulse on the transition $|B\rangle \rightarrow |-1_e,+\rangle$.

4.3 Step-by-step dark state pumping

The pulsed-CPT protocol described above is performed in an unusual regime for which relaxation from the excited level of the Λ-scheme is externally triggered through incoherent optical pumping and well-separated in time from coherent microwave excitations [46]. This CPT method with controlled dissipation can be used to investigate the dynamics of the sequential accumulation of population in the dark state. To this end, the CPT sequence including a dual microwave π-pulse followed by a laser pulse of duration T_L is repeated N times, as sketched in the inset of Fig. 6.

At the beginning of the N^{th} pumping sequence, the populations in the ground levels of the Λ-scheme, $|D\rangle$ and $|B\rangle$, are the one obtained at the end of the $(N-1)^{\text{th}}$ sequence, $\mathcal{P}_{|D\rangle}(N-1)$ and $\mathcal{P}_{|B\rangle}(N-1)$. Considering an ideal polarization of the NV defect in the $m_s = 0$ manifold by optical pumping, these populations are linked by $\mathcal{P}_{|D\rangle}(N-1) + \mathcal{P}_{|B\rangle}(N-1) = 1$. After applying the dual microwave π-pulse, the population in the excited-level $|-1_e,+\rangle$ is then given by

$$\mathcal{P}_{|-1_e,+\rangle}(N) = \mathcal{P}_{|B\rangle}(N-1) \tag{15}$$

such that the probability to find the spin system in the dark state simply reads

$$\mathcal{P}_{|D\rangle}(N-1) = 1 - \mathcal{P}_{|-1_e,+\rangle}(N). \tag{16}$$

The sequential accumulation of population in the dark state can thus be inferred by measuring the population in state $|-1_e,+\rangle$ through a spin-dependent PL measurement at each repetition of the CPT sequence [46]. Figure 6 shows the results of this experiment performed for different laser pulse durations T_L and a dual microwave excitation with $\Omega_1/\Omega_2 = 0.26$. Starting from a thermal state $\mathcal{P}_{|D\rangle}(0) = 1/2$, the population of the dark state increases exponentially with the number of CPT steps and reaches a steady-state value that corresponds to the efficiency of dark state pumping. Here, the polarization efficiency reaches $\sim 85\%$ for the shortest laser pulse duration $T_L = 300$ ns, and drops to $\sim 58\%$ when $T_L = 8$ μs. Such results are similar to the one reported in Sect. 3.2 (Fig. 3d).

These dynamics can be understood by considering the competition between (i) dark state pumping with a probability α_p per CPT step and (ii) nuclear spin dephasing induced by optical cycles, with a probability

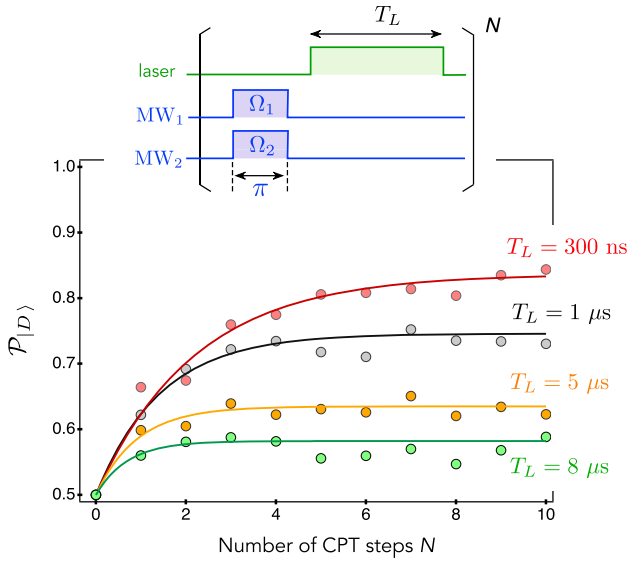

Fig. 6 Probability $\mathcal{P}_{|D\rangle}$ to find the ^{13}C nuclear spin in the dark state after N pumping steps (see inset) for a dual microwave π-pulse characterized by $\Omega_1/\Omega_2 = 0.26$. The experiment is performed for different durations T_L of the laser pulse used to trigger the relaxation of the Λ-scheme. The solid lines are data fitting with Eq. (19) from which the parameters α_p and α_{dp} are extracted

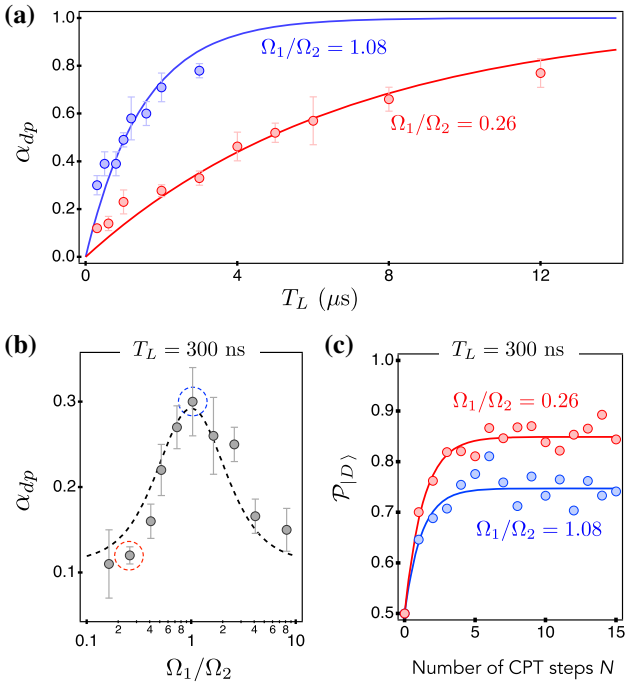

Fig. 7 **a** Probability α_{dp} as a function of the duration T_L of the laser pulse obtained for $\Omega_1/\Omega_2 = 0.26$ (red) and $\Omega_1/\Omega_2 = 1.08$ (blue). Solid lines are data fitting with Eq. (17). **b** Probability α_{dp} plotted as a function of Ω_1/Ω_2 on a semi-log scale for a laser pulse duration fixed to $T_L = 300$ ns. The black dashed line is a fit to the data using Eq. (20). **c** Probability $\mathcal{P}_{|D\rangle}$ to find the ^{13}C nuclear spin in the dark state after N pumping steps for a dual microwave π-pulse characterized by $\Omega_1/\Omega_2 = 0.26$ (red) and $\Omega_1/\Omega_2 = 1.08$ (blue) using $T_L = 300$ ns. Solid lines are data fitting with Eq. (19)

α_{dp} per step expressed as

$$\alpha_{dp} = 1 - \exp(-\Gamma_{dp} T_L) \tag{17}$$

where Γ_{dp} denotes the nuclear-spin dephasing rate under optical illumination. Using the simple rate equation model introduced in Ref. [46], the dark state population after N pumping steps can then be written as

$$\mathcal{P}_{|D\rangle}(N) = \frac{\alpha_p + \alpha_{dp}(0.5 - \alpha_p)}{\alpha_p + \alpha_{dp}(1 - \alpha_p)} \tag{18}$$

$$- 0.5 \frac{\alpha_p(1 - \alpha_{dp})}{\alpha_p + \alpha_{dp}(1 - \alpha_p)} \exp\left(-\frac{N}{N_s}\right), \tag{19}$$

where $N_s = -1/\ln[1 - \alpha_p - \alpha_{dp}(1 - \alpha_p)]$ is the characteristic number of pumping steps to reach the steady state.

Sequential dark state pumping experiments were fitted with Eq. (19) to infer the evolution of the parameter α_{dp} with the laser pulse duration T_L. As shown in Fig. 7a [red curve], α_{dp} increases exponentially with T_L. Data fitting with Eq. (17) leads to $\Gamma_{dp} = 0.14 \pm 0.01$ μs^{-1}. For these experiments, the dual microwave excitation is characterized by $\Omega_1/\Omega_2 \sim 0.26$ so that the dark state composition is close to a population state $|D\rangle \sim |0_e, \downarrow\rangle$ [see Eq. (14)]. As a result, the parameter Γ_{dp} extracted from these measurements mainly corresponds to the longitudinal nuclear spin relaxation time under optical illumination $T_{1,n}^{\text{laser}} \sim 1/\Gamma_{dp} = 7.0 \pm 0.4$ μs. The same experiments were then performed for a dual microwave excitation with $\Omega_1/\Omega_2 \sim 1.08$, yielding a much faster dephasing rate $\Gamma_{dp} = 0.66 \pm 0.05$ μs^{-1} (see Fig. 7a, blue curve). In this case, the dark state is close to an optimal coherent superposition $|D\rangle \sim \frac{1}{\sqrt{2}}(|0_e, \downarrow\rangle - |0_e, \uparrow\rangle)$. The dephasing rate Γ_{dp} is therefore linked to the transverse nuclear spin relaxation time under optical illumination $T_{2,n}^{\text{laser}} \sim 1/\Gamma_{dp} = 1.5 \pm 0.1$ μs. These results show that nuclear spin coherences are less robust than populations under optical illumination. This is further illustrated by Fig. 7b where the parameter α_{dp} is plotted as a function of Ω_1/Ω_2 for a fixed value of the laser pulse duration $T_L = 300$ ns. We observed that α_{dp} reaches a maximum for $\Omega_1/\Omega_2 \sim 1$. As a result, the polarization efficiency is reduced for dark states corresponding to a coherent superposition of the ^{13}C nuclear spin states (Fig. 7c).

The behavior observed in Fig. 7b can be modeled by considering a pure nuclear spin dephasing process with rate γ_d and a thermalization process or spin flips with a symmetric rate γ, both in the nuclear basis $\{|\uparrow\rangle, |\downarrow\rangle\}$ and under optical illumination. Using Bloch equation

formalism, the expected behavior for α_{dp} is given by

$$\alpha_{dp} T_L^{-1} \approx 2\gamma + 4(\gamma_d - \gamma) \left(\frac{\Omega_1/\Omega_2}{1 + (\Omega_1/\Omega_2)^2} \right)^2 . \quad (20)$$

Note that this equation is only valid for $\Gamma_{dp} T_L \ll 1$, such that $\Gamma_{dp} \approx \alpha_{dp} T_L^{-1}$ [see Eq. (17)]. Fitting the data shown in Fig. 7b with Eq. (20) leads to a thermalization rate $\gamma = 200 \pm 30$ kHz and a pure dephasing rate $\gamma_d = 790 \pm 80$ kHz. These two processes are expected for a nuclear spin interacting with an electronic spin via hyperfine interaction where both nuclear spin precession (due to $\mathcal{A}_{zz}$) and nuclear spin flips (due to $\mathcal{A}_{ani}$) might take place. Furthermore, the obtained rates are of the order of the hyperfine interaction terms for a nuclear spin of 'family I' (see Section IIIA). We finally note that these rates are related to the relaxation times $T_{1,n}^{\text{laser}}$ and $T_{2,n}^{\text{laser}}$ introduced above. Indeed, in the limit $\Omega_1/\Omega_2 \to 0$, only the thermalization rate γ plays a role leading to $\Gamma_{dp} \approx 2\gamma \sim 1/T_{1,n}^{\text{laser}}$. Meanwhile, when $\Omega_1/\Omega_2 = 1$, the thermalization rate γ and the pure dephasing rate γ_d participate, leading to $\Gamma_{dp} \approx \gamma + \gamma_d \sim 1/T_{2,n}^{\text{laser}}$.

5 Conclusion

To summarize, we have described two different methods providing room-temperature polarization of individual ^{13}C nuclear spins featuring a moderate hyperfine coupling strength (~ 1 MHz) with a single NV defect in diamond. For both approach, we have shown that the polarization efficiency remains limited by nuclear spin dephasing under optical illumination. The presented polarization and CPT techniques could be scaled up to more nuclei by using the hyperfine coupling between the NV electronic spin and the intrinsic ^{14}N nuclear spin under transverse magnetic fields [68]. These methods could find use for efficient quantum information storage of microwave photons in superconducting resonators [69], quantum metrology [47] and coherent control of nuclear spins through stimulated Raman adiabatic passage [70].

Acknowledgements We take the opportunity of this paper to warmly thank Alain Aspect for a large number of insightful scientific discussions over the last years. This research has been partially funded by the international cooperative program ECOS-CONICYT (Grant No. C16E04).

Author contributions

PJ and AD performed the experiments. All authors discussed and analyzed the data. VJ wrote the paper.

Data Availability Statement This manuscript has no associated data or the data will not be deposited. [The data that support the findings of this study are available from the corresponding author upon reasonable request.].

References

1. A. Aspect, John Bell and the second quantum revolution (in Speakable and unspeakable in quantum mechanics: Collected papers on quantum philosophy, Cambridge University Press, Cambridge, 2004) https://doi.org/10.1017/CBO9780511815676.002
2. B.E. Kane, Nature **393**, 133 (1998). https://doi.org/10.1038/30156
3. T. D. Ladd, F. Jelezko, R. Laflamme, Y. Nakamura, C. Monroe, J. L. O'Brien, Nature **464**, 45 (2010) http://www.nature.com/nature/journal/v455/n7213/abs/nature07279.html
4. D.R. McCamey, J.V. Tol, G.W. Morley, C. Boehme, Science **330**, 1652 (2010). https://doi.org/10.1126/science.1197931
5. M. Steger, K. Saeedi, M.L.W. Thewalt, J.J.L. Morton, H. Riemann, N.V. Abrosimov, P. Becker, H.-J. Pohl, Science **336**, 1280 (2012). https://doi.org/10.1126/science.1217635
6. T.W. Kornack, R.K. Ghosh, M.V. Romalis, Phys. Rev. Lett. **95**, 230801 (2005). https://doi.org/10.1103/PhysRevLett.95.230801
7. V.V. Soshenko, S.V. Bolshedvorskii, O. Rubinas, V.N. Sorokin, A.N. Smolyaninov, V.V. Vorobyov, A.V. Akimov, Phys. Rev. Lett. **126**, 197702 (2021). https://doi.org/10.1103/PhysRevLett.126.197702
8. A. Jarmola, S. Lourette, V.M. Acosta, A.G. Birdwell, P. Blümler, D. Budker, T. Ivanov, V.S. Malinovsky, Science Advances **7**, eabl3840 (2021). https://doi.org/10.1126/sciadv.abl3840
9. J. Randall, C.E. Bradley, F.V. van der Gronden, A. Galicia, M.H. Abobeih, M. Markham, D.J. Twitchen, F. Machado, N.Y. Yao, T.H. Taminiau, Science **374**, 1474 (2021). https://doi.org/10.1126/science.abk0603
10. R. Vincent, S. Klyatskaya, M. Ruben, W. Wernsdorfer, F. Balestro, Nature **488**, 357 (2012). https://doi.org/10.1038/nature11341
11. A. Bourassa, C.P. Anderson, K.C. Miao, M. Onizhuk, H. Ma, A.L. Crook, H. Abe, J. Ul-Hassan, T.

Ohshima, N.T. Son, G. Galli, D.D. Awschalom, Nature Mater. **19**, 1319 (2020). https://doi.org/10.1038/s41563-020-00802-6
12. F. Jelezko, T. Gaebel, I. Popa, M. Domhan, A. Gruber, J. Wrachtrup, Phys. Rev. Lett. **93**, 130501 (2004). https://doi.org/10.1103/PhysRevLett.93.130501
13. L. Childress, M.V. Gurudev Dutt, J.M. Taylor, A.S. Zibrov, F. Jelezko, J. Wrachtrup, P.R. Hemmer, M.D. Lukin, Science **314**, 281 (2006)
14. M. V. G. Dutt, L. Childress, L. Jiang, E. Togan, J. Maze, F. Jelezko, A. S. Zibrov, P. R. Hemmer, M. D. Lukin, Science **316**, 1312 (2007) http://www.sciencemag.org/cgi/content/abstract/316/5829/1312
15. P. Neumann, N. Mizuochi, F. Rempp, P. Hemmer, H. Watanabe, S. Yamasaki, V. Jacques, T. Gaebel, F. Jelezko, J. Wrachtrup, Science **320**, 1326 (2008). https://doi.org/10.1126/science.1157233
16. P. Neumann, J. Beck, M. Steiner, F. Rempp, H. Fedder, P.R. Hemmer, J. Wrachtrup, F. Jelezko, Science **329**, 542 (2010). https://doi.org/10.1126/science.1189075
17. P.C. Maurer, G. Kucsko, C. Latta, L. Jiang, N.Y. Yao, S.D. Bennett, F. Pastawski, D. Hunger, N. Chisholm, M. Markham, D.J. Twitchen, J.I. Cirac, M.D. Lukin, Science **336**, 1283 (2012). https://doi.org/10.1126/science.1220513
18. M.W. Doherty, N.B. Manson, P. Delaney, F. Jelezko, J. Wrachtrup, L.C. Hollenberg, Phys. Rep. **528**, 1 (2013). https://doi.org/10.1016/j.physrep.2013.02.001
19. G. Balasubramanian, P. Neumann, D. Twitchen, M. Markham, R. Kolesov, N. Mizuochi, J. Isoya, J. Achard, J. Beck, J. Tissler, V. Jacques, P.R. Hemmer, F. Jelezko, J. Wrachtrup, Nature Mater. **8**, 383 (2009). https://doi.org/10.1038/nmat2420
20. T.H. Taminiau, J. Cramer, T. van der Sar, V.V. Dobrovitski, R. Hanson, Nature Nanotechnol. **9**, 171 (2014). https://doi.org/10.1038/nnano.2014.2
21. G. Waldherr, Y. Wang, S. Zaiser, M. Jamali, T. Schulte-Herbrüggen, H. Abe, T. Ohshima, J. Isoya, J.F. Du, P. Neumann, J. Wrachtrup, Nature **506**, 204 (2014). https://doi.org/10.1038/nature12919
22. N. Kalb, A.A. Reiserer, P.C. Humphreys, J.J.W. Bakermans, S.J. Kamerling, N.H. Nickerson, S.C. Benjamin, D.J. Twitchen, M. Markham, R. Hanson, Science **356**, 928 (2017). https://doi.org/10.1126/science.aan0070
23. A. Reiserer, N. Kalb, M.S. Blok, K.J.M. van Bemmelen, T.H. Taminiau, R. Hanson, D.J. Twitchen, M. Markham, Phys. Rev. X **6**, 021040 (2016). https://doi.org/10.1103/PhysRevX.6.021040
24. S. Zaiser, T. Rendler, I. Jakobi, T. Wolf, S.-Y. Lee, S. Wagner, V. Bergholm, T. Schulte-Herbrüggen, P. Neumann, J. Wrachtrup, Nature Commun. **7**, 12279 (2016). https://doi.org/10.1038/ncomms12279
25. T. Rosskopf, J. Zopes, J.M. Boss, C.L. Degen, npj Quantum Inf. **3**, 33 (2017). https://doi.org/10.1038/s41534-017-0030-6
26. N. Aslam, M. Pfender, P. Neumann, R. Reuter, A. Zappe, F.F. de Oliveira, A. Denisenko, H. Sumiya, S. Onoda, J. Isoya, J. Wrachtrup, Science **357**, 67 (2017). https://doi.org/10.1126/science.aam8697
27. Z. Qiu, U. Vool, A. Hamo, A. Yacoby, npj Quantum Inf. **7**, 39 (2021). https://doi.org/10.1038/s41534-021-00374-6
28. N. Mizuochi, P. Neumann, F. Rempp, J. Beck, V. Jacques, P. Siyushev, K. Nakamura, D.J. Twitchen, H. Watanabe, S. Yamasaki, F. Jelezko, J. Wrachtrup, Phys. Rev. B **80**, 041201(R) (2009). https://doi.org/10.1103/PhysRevB.80.041201
29. J.R. Maze, A. Dréau, V. Waselowski, H. Duarte, J.-F. Roch, V. Jacques, New J. Phys. **14**, 103041 (2012). https://doi.org/10.1088/1367-2630/14/10/103041
30. N. Zhao, S.-W. Ho, R.-B. Liu, Phys. Rev. B **85**, 115303 (2012). https://doi.org/10.1103/PhysRevB.85.115303
31. A. Dréau, P. Jamonneau, O. Gazzano, S. Kosen, J.-F. Roch, J.R. Maze, V. Jacques, Phys. Rev. Lett. **113**, 137601 (2014). https://doi.org/10.1103/PhysRevLett.113.137601
32. A. Gali, Phys. Rev. B **80**, 241204 (2009). https://doi.org/10.1103/PhysRevB.80.241204
33. B. Smeltzer, L. Childress, A. Gali, New J. Phys. **13**, 025021 (2011) http://stacks.iop.org/1367-2630/13/i=2/a=025021
34. A. Dréau, J.-R. Maze, M. Lesik, J.-F. Roch, V. Jacques, Phys. Rev. B **85**, 134107 (2012). https://doi.org/10.1103/PhysRevB.85.134107
35. A.P. Nizovtsev, S.Y. Kilin, A.L. Pushkarchuk, V.A. Pushkarchuk, F. Jelezko, New J. Phys. **16**, 083014 (2014). https://doi.org/10.1088/1367-2630/16/8/083014
36. T.H. Taminiau, J.J.T. Wagenaar, T. van der Sar, F. Jelezko, V.V. Dobrovitski, R. Hanson, Phys. Rev. Lett. **109**, 137602 (2012). https://doi.org/10.1103/PhysRevLett.109.137602
37. S. Kolkowitz, Q.P. Unterreithmeier, S.D. Bennett, M.D. Lukin, Phys. Rev. Lett. **109**, 137601 (2012). https://doi.org/10.1103/PhysRevLett.109.137601
38. N. Zhao, J. Honert, B. Schmid, M. Klas, J. Isoya, M. Markham, D. Twitchen, F. Jelezko, R.-B. Liu, H. Fedder, J. Wrachtrup, Nature Nanotechnol. **7**, 657 (2012). https://doi.org/10.1038/nnano.2012.152
39. C.E. Bradley, J. Randall, M.H. Abobeih, R.C. Berrevoets, M.J. Degen, M.A. Bakker, M. Markham, D.J. Twitchen, T.H. Taminiau, Phys. Rev. X **9**, 031045 (2019). https://doi.org/10.1103/PhysRevX.9.031045
40. V. Jacques, P. Neumann, J. Beck, M. Markham, D. Twitchen, J. Meijer, F. Kaiser, G. Balasubramanian, F. Jelezko, J. Wrachtrup, Phys. Rev. Lett. **102**, 057403 (2009). https://doi.org/10.1103/PhysRevLett.102.057403
41. A. Dréau, P. Spinicelli, J.R. Maze, J.-F. Roch, V. Jacques, Phys. Rev. Lett. **110**, 060502 (2013). https://doi.org/10.1103/PhysRevLett.110.060502
42. J.S. Hodges, J.C. Yang, C. Ramanathan, D.G. Cory, Phys. Rev. A **78**, 010303 (2008). https://doi.org/10.1103/PhysRevA.78.010303
43. Y. Zhang, C.A. Ryan, R. Laflamme, J. Baugh, Phys. Rev. Lett. **107**, 170503 (2011). https://doi.org/10.1103/PhysRevLett.107.170503
44. J. Zhang, S.S. Hegde, D. Suter, Phys. Rev. Appl. **12**, 064047 (2019). https://doi.org/10.1103/PhysRevApplied.12.064047
45. J. Yun, K. Kim, D. Kim, New J. Phys. **21**, 093065 (2019). https://doi.org/10.1088/1367-2630/ab43aa
46. P. Jamonneau, G. Hétet, A. Dréau, J.-F. Roch, V. Jacques, Phys. Rev. Lett. **116**, 043603 (2016). https://doi.org/10.1103/PhysRevLett.116.043603

47. L. Nicolas, T. Delord, P. Jamonneau, R. Coto, J. Maze, V. Jacques, G. Hétet, New J. Phys. **20**, 033007 (2018). https://doi.org/10.1088/1367-2630/aab574
48. N.B. Manson, J.P. Harrison, M.J. Sellars, Phys. Rev. B **74**, 104303 (2006). https://doi.org/10.1103/PhysRevB.74.104303
49. A. Dréau, M. Lesik, L. Rondin, P. Spinicelli, O. Arcizet, J.-F. Roch, V. Jacques, Phys. Rev. B **84**, 195204 (2011). https://doi.org/10.1103/PhysRevB.84.195204
50. H. Duarte, H.T. Dinani, V. Jacques, J.R. Maze, Phys. Rev. B **103**, 195443 (2021). https://doi.org/10.1103/PhysRevB.103.195443
51. L. Robledo, H. Bernien, T. van der Sar, R. Hanson, New J. Phys. **13**, 025013 (2011). https://doi.org/10.1088/1367-2630/13/2/025013
52. L. Jiang, M.V.G. Dutt, E. Togan, L. Childress, P. Cappellaro, J.M. Taylor, M.D. Lukin, Phys. Rev. Lett. **100**, 073001 (2008). https://doi.org/10.1103/PhysRevLett.100.073001
53. E. Arimondo, V Coherent Population Trapping in Laser Spectroscopy, edited by E. Wolf, Progress in Optics, Vol. 35 (Elsevier, 1996) pp. 257–354 https://doi.org/10.1016/S0079-6638(08)70531-6
54. G. Alzetta, A. Gozzini, L. Moi, G. Orriols, Il Nuovo Cimento B (1971-1996) **36**, 5 (1976). https://doi.org/10.1007/BF02749417
55. E. Arimondo, G. Orriols, Lettere al Nuovo Cimento **17**, 333 (1976). https://doi.org/10.1007/BF02746514
56. H. R. Gray, R. M. Whitley, C. R. Stroud, Opt. Lett. **3**, 218 (1978) http://opg.optica.org/ol/abstract.cfm?URI=ol-3-6-218
57. A. Aspect, E. Arimondo, R. Kaiser, N. Vansteenkiste, C. Cohen-Tannoudji, Phys. Rev. Lett. **61**, 826 (1988). https://doi.org/10.1103/PhysRevLett.61.826
58. K.-K. Ni, S. Ospelkaus, M.H.G. de Miranda, A. Pe'er, B. Neyenhuis, J.J. Zirbel, S. Kotochigova, P.S. Julienne, D.S. Jin, J. Ye, Science **322**, 231 (2008). https://doi.org/10.1126/science.1163861
59. M.O. Scully, M. Fleischhauer, Phys. Rev. Lett. **69**, 1360 (1992). https://doi.org/10.1103/PhysRevLett.69.1360
60. J. Vanier, Appl. Phys. B **81**, 421 (2005). https://doi.org/10.1007/s00340-005-1905-3
61. D.F. Phillips, A. Fleischhauer, A. Mair, R.L. Walsworth, M.D. Lukin, Phys. Rev. Lett. **86**, 783 (2001). https://doi.org/10.1103/PhysRevLett.86.783
62. C. Liu, Z. Dutton, C. H. Behroozi, L. V. Hau, Nature **409**, 490 (2001) https://www.nature.com/articles/35054017
63. X. Xu, B. Sun, P.R. Berman, D.G. Steel, A.S. Bracker, D. Gammon, L.J. Sham, Nature Phys. **4**, 692 (2008). https://doi.org/10.1038/nphys1054
64. K. Xia, R. Kolesov, Y. Wang, P. Siyushev, R. Reuter, T. Kornher, N. Kukharchyk, A.D. Wieck, B. Villa, S. Yang, J. Wrachtrup, Phys. Rev. Lett. **115**, 093602 (2015). https://doi.org/10.1103/PhysRevLett.115.093602
65. C. Santori, P. Tamarat, P. Neumann, J. Wrachtrup, D. Fattal, R.G. Beausoleil, J. Rabeau, P. Olivero, A.D. Greentree, S. Prawer, F. Jelezko, P. Hemmer, Phys. Rev. Lett. **97**, 247401 (2006). https://doi.org/10.1103/PhysRevLett.97.247401
66. W.R. Kelly, Z. Dutton, J. Schlafer, B. Mookerji, T.A. Ohki, J.S. Kline, D.P. Pappas, Phys. Rev. Lett. **104**, 163601 (2010). https://doi.org/10.1103/PhysRevLett.104.163601
67. S. Novikov, T. Sweeney, J.E. Robinson, S.P. Premaratne, B. Suri, F.C. Wellstood, B.S. Palmer, Nature Physics **12**, 75 (2016). https://doi.org/10.1038/nphys3537
68. P. Huillery, J. Leibold, T. Delord, L. Nicolas, J. Achard, A. Tallaire, G. Hétet, Phys. Rev. B **103**, L140102 (2021). https://doi.org/10.1103/PhysRevB.103.L140102
69. C. Grezes, B. Julsgaard, Y. Kubo, M. Stern, T. Umeda, J. Isoya, H. Sumiya, H. Abe, S. Onoda, T. Ohshima, V. Jacques, J. Esteve, D. Vion, D. Esteve, K. Mølmer, P. Bertet, Phys. Rev. X **4**, 021049 (2014). https://doi.org/10.1103/PhysRevX.4.021049
70. R. Coto, V. Jacques, G. Hétet, J.R. Maze, Phys. Rev. B **96**, 085420 (2017). https://doi.org/10.1103/PhysRevB.96.085420